Article

Nitrogen-Enriched Carbon Nanobubbles and Nanospheres for Applications in Energy Harvesting, Storage, and CO$_2$ Sequestration

Devika Laishram,[‡] Kiran P. Shejale,[‡] R. Krishnapriya, and Rakesh K. Sharma*

Read Online

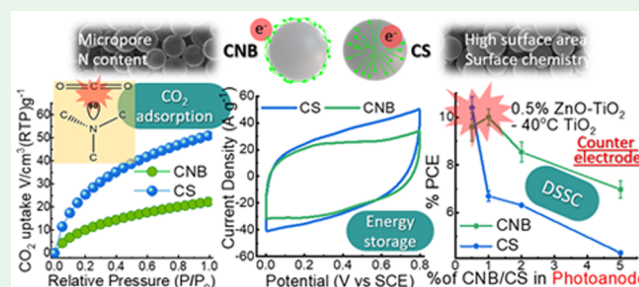ACCESS | Metrics & More | Article Recommendations | SI Supporting Information

ABSTRACT: Multifunctional carbon nanomaterials have attracted remarkable consideration for use in various energy conversion and storage devices because of their ultrahigh specific surface area, unique morphology, and excellent electrochemical properties. Herein, we report the synthesis of highly uniform and ordered nitrogen-enriched carbon nanospheres (CS) and nanobubbles (CNB) by a modified Stöber reaction using resorcinol and formaldehyde in the presence of ethylenediamine as a nitrogen source. A comparative study of the prepared CS and CNB nanomaterials is presented here with potential use in a wide variety of applications involving large surface area and electrical conductivity. As counter electrode materials in solar cells, CNB and CS showed enhanced photoelectrochemical activity for catalytically reducing I$_3^-$ to I$^-$ and improved capacitive behavior with a low charge transfer resistance and remarkable power conversion efficiency (PCE) of 10.40% with improved J_{sc} (20.20 mA/cm^2) and V_{oc} (0.73 V). The enhanced performance of the fabricated photoelectrochemical cell is due to the excellent point contact and good conductivity that offered better charge transportation of electrons with minimum recombination. The enhanced adsorption upon increasing the pressure without an apparent saturation level signified the large CO$_2$ adsorption with 2 mmol/g for the CS. Additionally, the rectangular-shaped CV curve indicated the double-layer capacitive behavior, good electrochemical reversibility, and high-power characteristics, prerequisites for supercapacitor application. This study probes the practical possibility of nitrogen-enriched carbon nanostructures as a multifunctional material for prospective applications.

KEYWORDS: nitrogen-doped carbon nanobubbles, carbon sphere, CO$_2$ adsorption, supercapacitor, dye sensitized solar cells (DSSC)

INTRODUCTION

Alternative renewable energy is an imperative today with the need to find a sustainable energy source with a smaller carbon footprint. The pragmatic approach toward tapping the solar and its tributary sources such as wind and hydro-energy is via conversion of this energy form, storing for later use and its transmission without significant losses. Additionally, materials and devices are required to remedy various environmental issues such as water pollution, CO$_2$ emission, etc. Therefore, the core for various device operations, which is the material component and in particular the electrode material, is the crucial determiner for enhanced performance of many energy conversion and storage devices such as supercapacitors and solar cells. High performing nanomaterials that are economically viable and ecologically benign are intriguing as these will bring about great changes to solve the energy crisis and fix other environmental issues. Oxides of precious metals such as Pt, Ru, Pd, Ir, and Rh have been found to limit the practical application due to their high cost despite its high performance.[1] Photoanodes for solar cell applications such as dye-sensitized solar cells (DSSC) reveal that the use of carbon-based nanomaterials such as SWCNTs, MWCNTs, and graphene increase the electrocatalytic activity and conductivity.[2−6]

However, in spite of improvements in certain aspects such as photocurrent generation, there remain certain drawbacks that abase the efficiency of a fabricated device. For example, the use of SWCNTs along with TiO$_2$ does not improve the performance of the device as it delivers lower photovoltage because of the discrepancy in the Fermi levels of TiO$_2$ and SWCNTs.[7] Using MWCNTs along with TiO$_2$ showed an escalation in the DSSC performance device due to enhancement in roughness factor and charge recombination process. Even so, beyond an optimal range, the MWCNTs negatively affect cell performance as they hinders absorbance of the dye itself.[8] Outside of these reasons, CNTs generally do not have
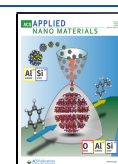
good point contact due to structural and morphological differences.[9]

Over the past decade the diverse morphology of nitrogen-doped carbon—cubes, fibers, and solid and hollow spheres—has seized great research attention because of the versatility that allows it to be used in a wide range of applications in the field of energy storage,[10−12] CO_2 capture[13] and storage,[14] and to some extent energy conversion.[15] For example, Liu et al. used hollow carbons for high performing Li-ion batteries by confining Sn inside the double shell.[16] Additionally, other applications best explored for these N-doped carbon materials include heavy metal adsorption[17] and biomedical applications.[18] Nitrogen doping in carbon-based nanostructures offers basic properties that enhance the interactions between the carbon surface and acid molecules. Thus, it can facilitate the adsorption of "Lewis acidic species" such as oxygen and carbon dioxide molecules. Moreover, it can alter the electronic and crystalline structures of the carbons which result in the improvement of chemical stability, surface polarity, electric conductivity, etc. The doping can also induce more disordered graphitic structure and could inhibit the formation of micropores in carbon structures.[19−21] Among these various forms, carbon hollow spheres are under vital consideration due to their salient features with controlled inner and outer shells with improved surface properties.[22] N-Doped carbon spheres as counter electrodes for DSSC have been previously reported to be a good catalyst for having the provision of donating electrons.[23] However, utilization of N-doped carbon based nanomaterials as a photoanode for applications pertaining to DSSC is still at the exploratory stage.

In this study, N-doped carbon nanospheres and N-doped carbon hollow nanospheres are used as support material in DSSC fabrication by using other metal oxides such as ZnO and TiO_2 reported earlier in our work.[24,25] Significant advances have been made toward the development of a graphitic film of TiO_2 for enhanced electrical conductivity.[3] Other hybrid mixtures of carbon allotropes along with TiO_2 are reported to increase the power conversion efficiency in DSSC, due to increased electron transport in the TiO_2 layer.[26,27]

In this study, synthesized carbon nanospheres and carbon nanobubbles are used in integration along with highly efficient variations of TiO_2 having different morphology, namely, oval-shaped anatase TiO_2 synthesized at subzero temperature and spherical heterostructure TiO_2 doped with 1% ZnO.[24,25] The introduction of carbon nanospheres is expected to promote dispersion, and the TiO_2 nanoparticles will display less agglomeration. Additionally, this will lead to a compounded enhancement of porosity, scattering of the light which will improve the amount of light, and dye absorption in the case of DSSC fabrication. It can also be projected to have new pathways for electron absorption and transport that will stimulate an increase in current density in the fabricated device. This study is a highlight of the differences of hollow carbon nanobubbles (CNB) and solid carbon spheres (CS). Illustrations of diverse and significant properties of these synthesized materials focusing on the chemical, physical, and morphological architecture have been detailed using various techniques, and consequently, the effect of these nanomaterials when used for applications pertaining to electrode materials for DSSC and supercapacitor application and as an adsorbent for CO_2 adsorption has been thoroughly examined.

■ EXPERIMENTAL DETAILS

Materials. Resorcinol and formaldehyde (37 wt %) were purchased from Qualigens and Fischer, respectively. Ethylenediamine (EDA), tetraethylorthosilicate (TEOS), and hydrofluoric acid (50 wt %) were obtained from Sigma-Aldrich. Ethanol was purchased from Shangzu, China. Ammonia was obtained from Qualigens. All chemicals were used without any further purification.

Preparation of Carbon Spheres (CS). An aliquot of 0.6 mL of EDA was added to a volume of ethanol and DI H_2O (mixed in 2:5 ratio) which is stirred until complete dissolution.[14,28] To it was added 0.4 g of resorcinol and 0.6 mL of formaldehyde (37 wt %). This system was kept stirring for 24 h at 30 °C. The content is then transferred to a steel-lined autoclave having a volume of 125 mL and kept in an oven at 100 °C for 24 h. After which, it is centrifuged at 10000 rpm at −6 °C for 15 min. The precipitate is collected and dried in air for 12 h. Annealing is done under N_2 atmosphere at 600 °C for 2 h.

Preparation of Carbon Nanobubbles (CNB). A 3.2 mL aliquot of liquor ammonia solution and 3 mL of TEOS were added to DI H_2O and ethanol mixed in a ratio 7:1. To this reaction mixture 0.21 g of resorcinol, 0.31 mL of formaldehyde (37 wt %), and 0.10 mL of EDA were added subsequently. The remaining process is similar to the preparation of CS. Finally, after annealing etching was performed using HF (50 wt %) solution, the nanobubbles were then washed with ethanol followed by drying at 50 °C for 12 h.

Electrode and Device Fabrication. All solar cells (DSSCs) were fabricated by a similar procedure as mentioned in our previous study.[24] CNB and CS are individually mixed with our previously reported ZnO doped TiO_2 and TiO_2 synthesized at −40 °C as a wt %. However, CNB and CS loading % were varied, such as 0.5, 1, 2, and 5%. CNB and CS based counter electrodes were prepared by a screen printing suspension of Nafion/ethanol (1:1) and synthesized carboneous nanoparticles and annealed at 450 °C in air for 30 min after overnight drying in air at room temperature.

A standard three-electrode setup was used to analyze the electrochemical performance of both materials: Pt mesh as a counter electrode, SCE (saturated calomel electrode) as a reference electrode, and the prepared materials as the working electrode. For the working electrode, the as-synthesized sample, polyvinylidene difluoride (PVDF), and carbon black at a ratio of 8:1:1 (weight ratio) in the presence of 1-methyl-2-pyrrolidone (NMP) were mixed and pasted on a carbon sheet and subsequently dried at 100 °C for 12 h.

Characterization. Brunauer−Emmet−Teller (BET) method for N_2 adsorption−desorption was performed to measure the specific surface area using the Quantachrome Autosorb iQ3 instrument. The as-synthesized carbon materials were subjected to degassing for 120 min at 150 °C to remove all the impurities from the pore. The morphological analysis was performed using field emission scanning electron microscopy (FESEM) and a transmission electron microscope (TEM) from FEI Tecnai-G2 T20. Raman spectra were acquired using the Avalon Instruments Raman Station R3 using an excitation laser source with 532 nm wavelength and a power density of 50 milliwatt μM^{-2}. The X-ray diffraction (XRD) pattern was recorded in the Bruker D8 Advance diffractometer equipped with Cu Kα radiation. XPS measurements were conducted to study the chemical and surface compositions in the synthesized material using a monochromatic Al Kα radiation equipped Omicron Nanotechnology from Oxford Instruments. TG analysis was carried out in a PerkinElmer, simultaneous thermal analyzer (STA) from room temperature to 900 °C at 10 C/min under N_2 atmosphere. I-V for the DSSC and other electrochemical measurements were recorded using the CHI660e from CH Instruments under one sun irradiation by PET Photo Emission Technology SS50AAA solar simulator. The supercapacitor performance was estimated by cyclic voltammetry (CV), electrochemical impedance spectroscopy (EIS), and galvanostatic charge−discharge techniques (0.1 mM Na_2SO_4 as an electrolyte, scan rate 100 mV/s, and applied voltage 0−1 V). CO_2 adsorption measurements of the synthesized materials were carried out after

Scheme 1. Schematic Illustration of the Reaction Mechanism of CS and CNB Formation by Modified Stöber Reaction[a]
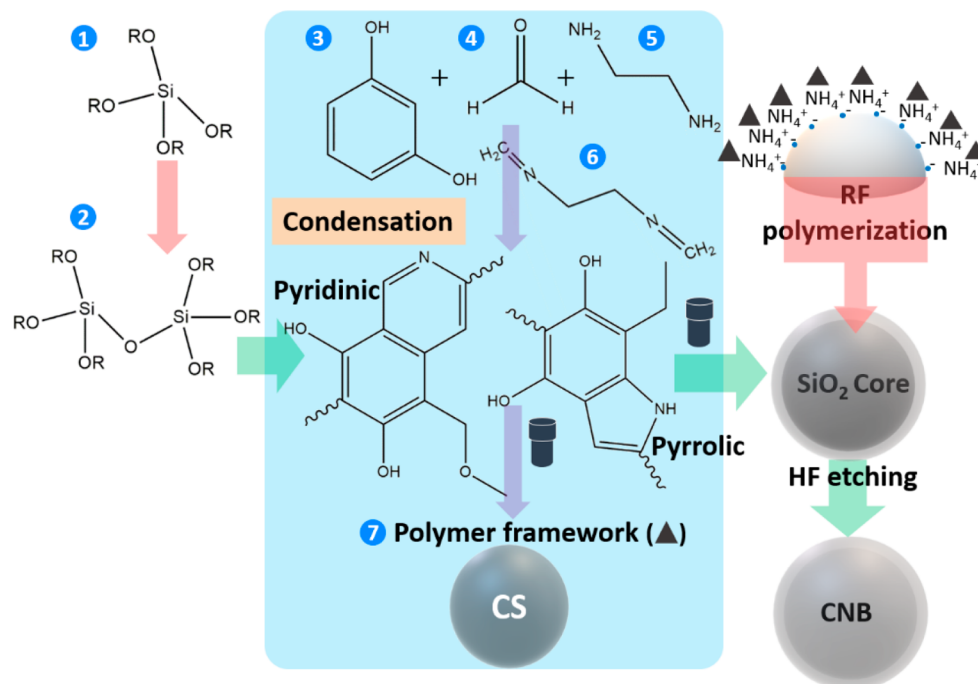
[a]The numeric labels indicate (1) Si(OR)$_4$, (2) 3D Si-polymer network, (3) resorcinol, (4) formaldehyde, (5) ethylenediamine (EDA), (6) intermediate compound of (4), (5), and (7) after excess reaction in between (3) and (4) forms polymer framework.

outgassing the materials for 12 h at 200 °C using Quantachrome Autosorb iQ3 at 298 K.

RESULTS AND DISCUSSION

A schematic illustration of the synthesis of nano CS and CNB by a Stöber reaction is given in Scheme 1.[29] The first step in the synthesis of ordered carbon nanospheres is the formation of emulsion drops via hydrogen bonding of the solvents using the precursors EDA, ethanol, water, formaldehyde, and resorcinol (1 to 7 in Scheme 1).[14] Here, EDA is used as a nitrogen source and also as the base catalyst. The ratio of water and ethanol is used to tune the size of the spheres as mentioned in the Experimental Details section. The next step of the reaction is the formation of a resin of resorcinol (3) and formaldehyde (4) by polymerization. After which an intermediate of the EDA–formaldehyde derived compound (6) gets integrated into the excess resorcinol–formaldehyde network forming the solid polymer spheres.[30] The resorcinol and formaldehyde reaction form a polymer framework (7) consisting of pyrrolic and pyridinic-type rings. The hydrothermal treatment of the polymer for 24 h led to the formation of uniform colloidal spheres. Finally, a carbonization step of annealing under nitrogen atmosphere results in the formation of carbon nanospheres (CS). This is a modified Stöber reaction, illustrated in Scheme 1. The similar reaction mechanism was adopted for the synthesis of hollow carbon nanobubbles (CNB) whereby TEOS was hydrolyzed and condensed (see compounds (1) and (2)) to form the core, and the RF resin acted as the carbon precursor covering the outer shell.[31,32] The reaction between the resorcinol and formaldehyde (7) results in intermediates diffusing on the surface, an effect of the presence of NH$_4^+$, results in the formation of a polymeric resin sphere.[33,34] A stable colloidal suspension of the negatively charged sphere surrounded by positively charged

NH$_4^+$ is formed, the interaction of which stabilizes and prevents the spheres from agglomerating.[28] Further, after the hydrothermal reaction, core SiO$_2$ is etched by HF with the above carbonization step to obtain hollow carbon nanobubbles.

The synthesized nanomaterials were subjected to morphological analysis using FESEM and TEM to confirm the formation of hollow carbon nanobubbles (CNB) and solid carbon nano pheres (CS). FESEM images at different magnification can be observed for both CNB and CS in Figure 1a,b,c and Figure 1d,e,f respectively, indicating the uniform distribution of the synthesized nanomaterials. The hollow nature of the CNB can be established from the higher magnification images in Figure 1b,c whereby the underlying spherical layers can be seen through the transparent spheres of the first layers unlike for CS in Figure 1e,f. This result is furthermore segmented by the TEM results in Figure 2a,b, showing hollow CNB against solid CS in Figure 2d,e. To realize the change in the pore structure of CS and CNB, N$_2$ adsorption–desorption BET was performed and the pore size was estimated using the Brauner–Joyner–Halenda (BJH) method (Figure 1g,h). Both CS and CNB showed an H4 type hysteresis loop with an isotherm similar to type I. This indicates that the synthesized nanomaterials are microporous. The filling of micropore type observes high uptake at relatively low pressure because of high adsorption potential due to the narrow pore structure as shown in the inset of Figure 1g,h. The hysteresis did not show any limiting absorption at high P/P_O with narrow pores with slits even within the micropores.

The hysteresis loop at low pressure is possibly due to swelling of nonrigid pores and uptake of adsorbent molecules with pore sizes similar to that of the adsorptive molecule.[35] Additionally, the high uptake observed at relatively low pressure in both cases is an indication of the presence of
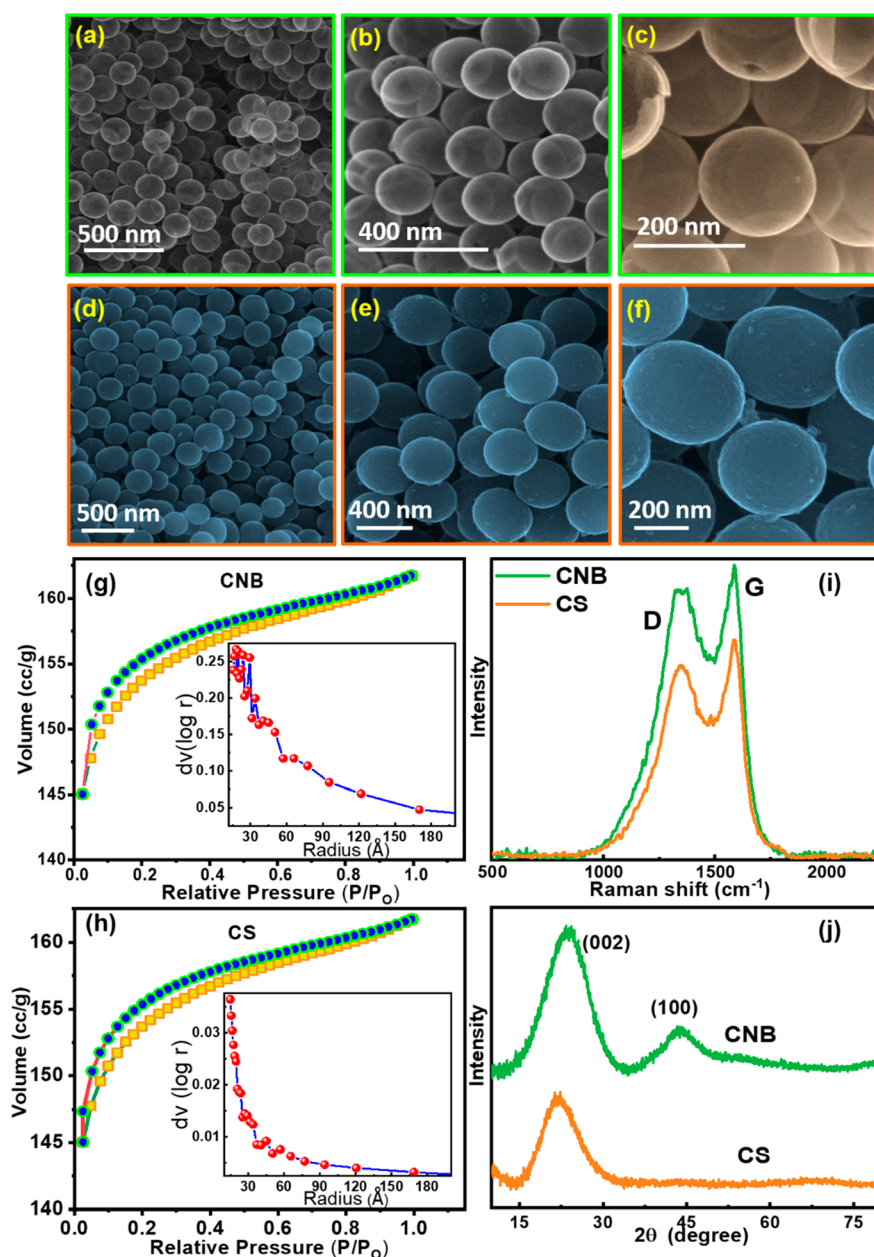
Figure 1. FESEM at different magnifications of (a, b , and c) CNB and (d, e, and f) CS, N_2 adsorption and desorption isotherms of (g) CNB and (h) CS with their respective pore size distribution (inset) in the range of 0.0 to 1.0 relative presses, (i) Raman and (j) XRD pattern (scan rate 0.1°/min).

nanopores within the shell.[36] Analysis of the surface area revealed CS to have a higher surface area with 468 m^2/g and pore volume of 0.25 cm^3/g while CNB were found to have reduced surface area at 360 m^2/g with pore volume 0.32 cm^3/g. Additionally, the average pore radius was calculated to be 1.7 nm for CNB, whereas the CS showed smaller pore radius size of around 1.0 nm. While it is expected for CNB to have greater surface area than the CS due to their ascertained hollow nature, it was found to be otherwise so. This can be due to the average size of the CS being much larger than that of the CNB as observed by the TEM image in Figure 2. Moreover, solid CS with 0.25 cm^3/g pore volume exhibited an aporous nature with the surface area capacity of 468 m^2/g. Thus, the higher amount of N_2 adsorption observed in the BET adsorption desorption isotherms for CS can be attributed to the larger size and the porous nature of the individual spheres.

Raman spectroscopy is an important method of characterization for carbon nanomaterials. The observed spectra (Figure 1i) showed two peaks distinct to the D and G band at 1347 and 1588 cm^{-1}. The presence of the D band is assigned to disordered amorphous carbon, whereas the G band is due to the in-plane vibrations of crystalline graphitic carbon. The ID/IG for CS is 0.97 and for the CNB is 1.18, which depicts the increasing defects on the latter.[37] The XRD peak (Figure 1j) for CS showed a broad peak at 21.86°, which can be attributed to low crystallinity and the amorphous presence of carbon. Whereas for the CNB two peaks were absorbed at 43.77°, 23.72° which corresponds to (100) and (002) planes which can be attributed to more carbonization at the CNB.[38] It can be observed from Figure 2b,e that the etching process performed using HF occurred within the inner part of the silica spheres without affecting the outer shell thickness
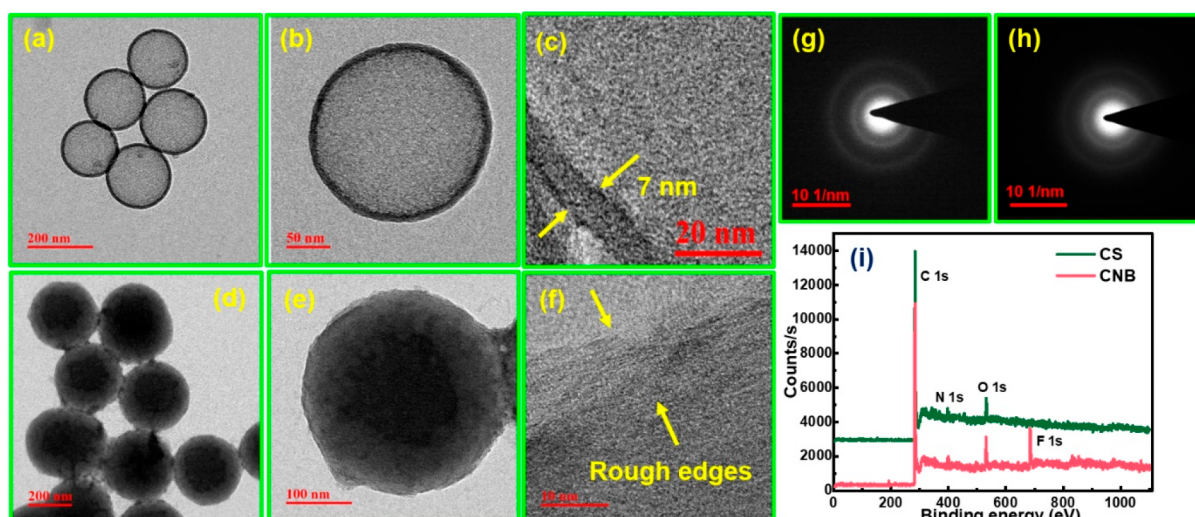
Figure 2. TEM images of group, single, and HRTEM of CNB (a−c) with shell (7 nm) and CS (d−f) with respective SAED pattern (g, h). (i) XPS survey spectra of CNB and CS.
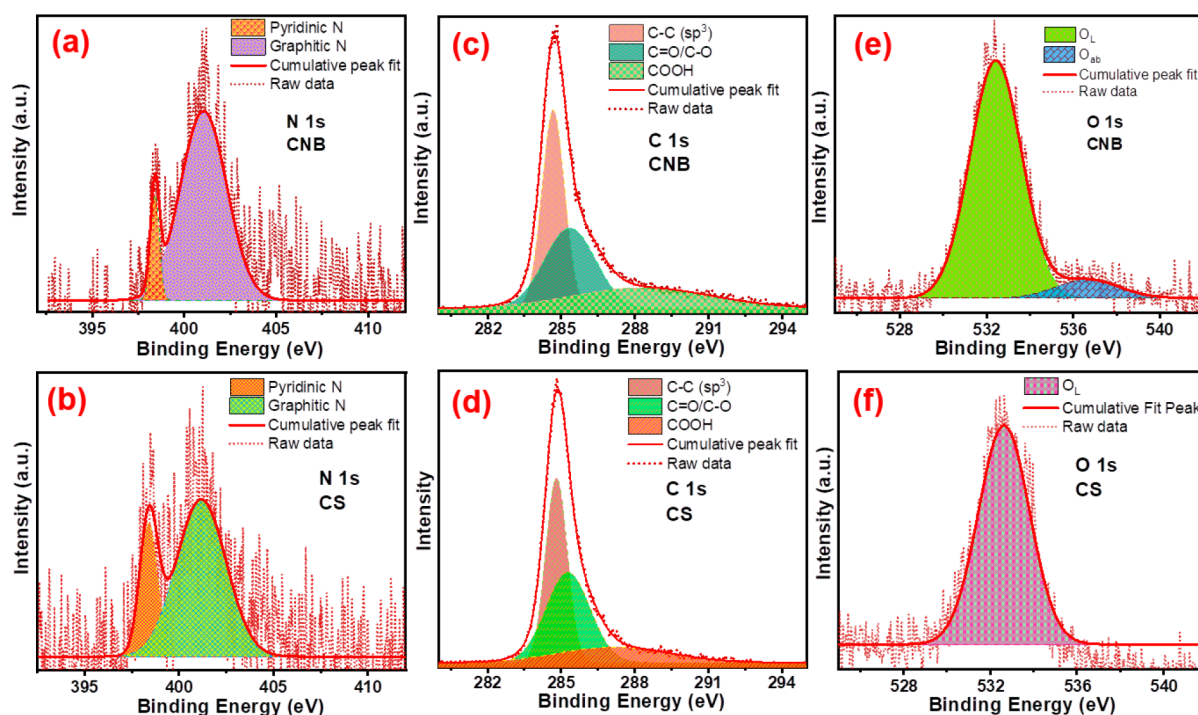

Figure 3. High resolution XPS spectra of N 1s (a, b), C 1s (c, d) and O 1s (e, f) of the synthesized CNB and CS, respectively.

measuring ∼7 nm as indicated in Figure 2c. However, the decrease in the average diameter size in CNB to ∼195 nm when compared to ∼320 nm of CS might suggest etching of outer periphery in CNB during the process. Furthermore, there is no defined shell. However, rough edges surrounding the CS can be observed from Figure 2f, which is also evidenced by the light gray color in the outer area surrounding a dark center in Figure 2e. Both the SAED patterns in Figure 2g,h suggest the amorphous nature of both CS and CNB as depicted in the XRD in Figure 1d.

Further differences are observed in the decomposition of CNB and CS from the TG analysis curves as displayed in Figure S1, Supporting Information. The CNB showed decomposition at an initial temperature below 100 °C due to the presence of water vapor and moisture inside the hollow

spheres. Furthermore, while both nanomaterials completely pyrolyze at 700 °C, the CS sample showed deferred reaction which might be due to the presence of the polymer sphere delaying the reaction of organic molecules present in the matrix and the carrier gas, that is, N_2 gas.[39] The CNB with a hollow core and outer shell were etched by HF solution. The XPS survey scan in Figure 2i confirms the presence of C, N, and O except for the presence of F in the CNB which might be because of the F^- ion remaining from the HF.

Additionally, functional groups present were identified using FTIR measurement (Figure S2, Supporting Information), and it can be observed that the IR peaks indicate the presence of similar functional groups. In both the carbon nanomaterials, vibrations bands relating to C=O and C=C were observed in bands 1700 cm^{-1} and −C−OH stretching bands were

observed at bands around 1300 cm^{-1}. Apart from this, hydroxyl bands were observed for the CNB at around 3500 cm^{-1} which might be the water molecules trapped in the hollow core of the CNB. This exhibition of a large number of functional groups stalls the presence of N containing groups occur in a similar region of the IR spectra. For example, C−N stretching occurring at around 1560 cm^{-1} is masked due to the presence of broad aromatic C=C at the region around 1600 cm^{-1}.[14] Similar overlap was observed for NH$_2$ vibration with the hydroxyl groups at around 3500 cm^{-1}.[40] Thus, the presence of N containing groups is not well resolved due to the overlap. Additionally, an increase in absorption at a region around 1600−1700 cm^{-1} might be due to the increase in the C−N aromatic stretching.

To better understand the chemical states of these carbon nanomaterials, XPS measurements were carried out (Figures 2i and 3). The high-resolution scan of N 1s XPS peaks were fitted using a Gaussian function to two peaks corresponding to pyridinic N and graphitic N at approximately 398.4 and 401 eV for both CNB and CS as shown in Figure 3a,b. The peak occurring at 401 eV can be assigned to graphitic or quaternary N. The integrated peak areas for the respective N species are given in Table 1, and it can be observed that there is a change

Table 1. Distribution of the N Components in the Synthesized Nanomaterials[a]

sample	pyridinic N		graphitic N	
	area (%)	BE (eV)	area (%)	BE (eV)
CS	23.31	398.40	76.69	401.17
CNB	9.51	398.41	90.49	401.05

[a]% area is the calculated area under the deconvoluted curve, and BE is the binding energy.

in the peak areas suggesting a change in the N bonding sites during the formation of CS and CNB. The % proportions of the pyridinic N decreases for CNB, whereas quaternary and graphitic N increases. The quaternary N is reported to increase the conductivity of carbon nanomaterial, whereas pyridinic N increases the pseudocapacitive effect and thus might be interesting for applications related to supercapacitors. Thus, CNB might contribute toward better charge transport.[11] Similarly, in Figure 3c,d, the high-resolution C 1s spectra showed three peaks after deconvolution centered around 284.6 and 284.8 eV for CNB and CS that can be assigned to sp^2 hybridized nonoxygenated C that is, C=C−C. While the

peaks at 285.36 eV for the CNB and 285.28 eV for the CS can be attributed to C−O/C−N. The peak at higher binding energies 288.3 and 287.16 eV corresponds to the carboxylate carbon (C=O), respectively for CNB and CS.[12,41] The O species present at 532.4 and 536.6 eV for CNB and 532.64 eV for CS can be ascribed to the lattice oxygen and adsorbed oxygen species present as shown in Figure 3e,f.[41] The XPS and FTIR establishes the presence of nitrogen content in the carbon nanomaterials and thus it can be explored for applications relating to CO$_2$ capture.

Measurements relating to CO$_2$ adsorption were carried out using Quantachrome Autosorb iQ3. The samples were outgassed for 12 h at 200 °C to remove impurities, moisture, and other molecules before the start of the adsorption experiment. CO$_2$ adsorption was performed by measuring the adsorption isotherms of the CS and CNB samples, and the observed parameters are summarized in Table S1, Supporting Information. As observed from the adsorption isotherm in Figure 4a,b the CO$_2$ uptake was fast at low pressure and increasing the pressure resulted in increased absorption. There was no apparent saturation level suggesting that there is still capacity to absorb at higher pressure. The porous nature, large surface to volume and nitrogen doping in the synthesized carbon nanomaterials will be viable for use in CO$_2$ capture applications. The CO$_2$ adsorption isotherms showing the capacity of adsorption at standard room temperature and pressure for CNB and CS and the number of cycles against the uptake are indicated in Figure 4 panels a and b, respectively. On comparison, the CS have stronger and steeper adsorption than the CNB counterpart starting from very low pressure. Neither carbon nanomaterials saturated even at high relative pressure, indicating the chances for more adsorption taking place at higher pressure[42] and showing the strong adsorption between the carbon nanospheres and CO$_2$ molecules. The adsorption capacity for CS and CNB samples was observed to be around 2 mmol/g and 1 mmol/g, respectively. The better adsorption in CS compared to CNB can be attributed to the increased N content that helps to increase the basic nature of the former by changing the surface chemistry, high surface area, and an increase in the micropore volume.[13,43] There is the possibility of a carbon atom in the CO$_2$ molecule binding strongly with lone pairs of electrons existing in the N groups in the carbon framework due to its electron-deficient nature.[40] As observed, the better CO$_2$ adsorbing CS-based carbon nano-material reports a higher pyridinic N; (from the XPS data in
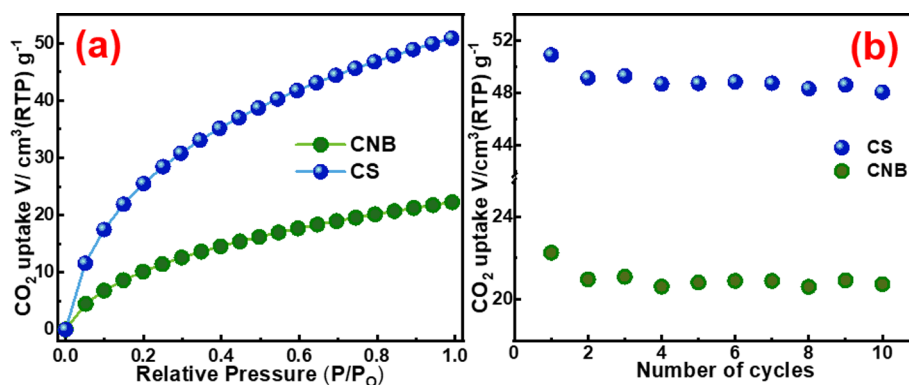

Figure 4. CO$_2$ adsorption (a) and cycle stability (b) of both the synthesized CS and CNB at 298 K.

Table 2. Photovoltaic DSSC Data Obtained from $I-V$ and EIS

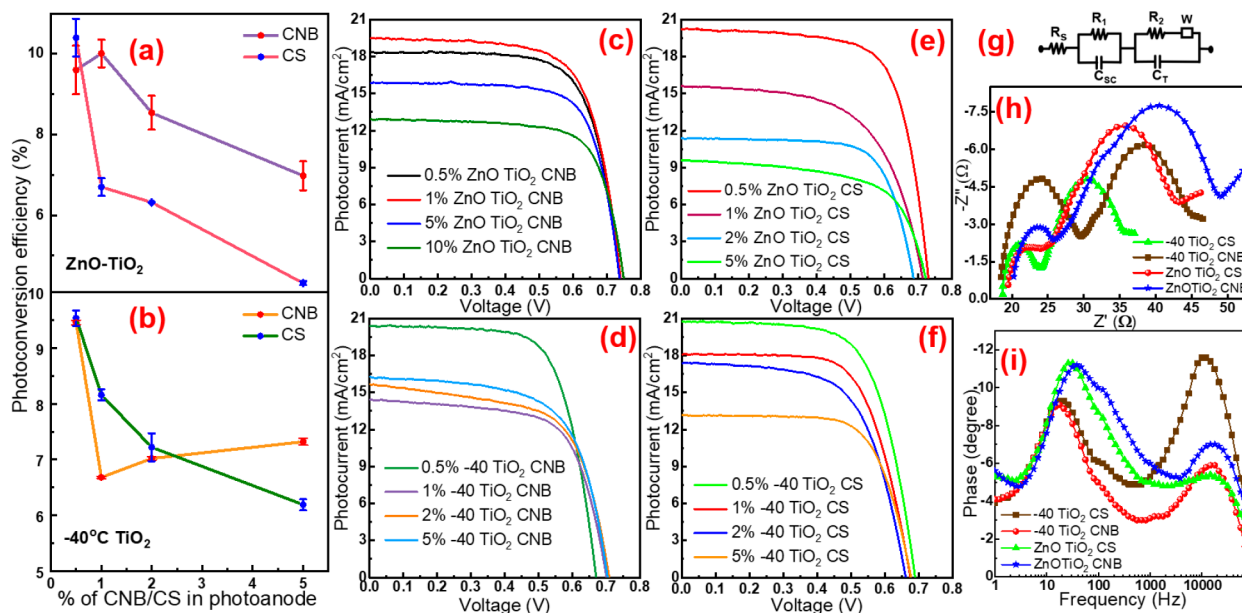| sample	V_{OC} (V)	J_{SC} (mA/cm^2)	PCE, η (%)	FF (%)	R_S (Ω)	R_1 (Ω)	R_2 (Ω)	C_{SC}	C_T	τ (ms)
0.5% CNB + ZnO−TiO$_2$	0.75	19.47	9.6	65.56	20.62	10.61	0.11	2.50×10^{-4}	2.27×10^{-6}	26
0.5% CS + ZnO−TiO$_2$	0.73	20.20	10.40	70.14	22.96	12.97	4.81	2.58×10^{-4}	4.52×10^{-6}	32
0.5% CNB + −40_TiO$_2$	0.67	20.37	9.46	68.59	22.96	15.08	10.44	5.35×10^{-4}	2.47×10^{-6}	46
0.5% CS + −40_TiO$_2$	0.70	20.75	9.54	66.05	18.77	8.97	5.06	8.64×10^{-4}	3.35×10^{-6}	56

Figure 5. Device parameters of fabricated DSSCs using the synthesized nanomaterials (dye N719, 0.5 mM and active area 0.04 cm^2). (a, b) Plot summing up the PCE of increasing loading% of CNB- and CS-based photoanodes with our earlier reported nanomaterial.[24,25] $I-V$ graphs of the synthesized CNB and CS in combination with different% ZnO doped TiO$_2$ (c, e) and TiO$_2$ synthesized at −40 °C (d, f), equivalent model circuit used in fitting (g), Nyquist plot (h, and bode plot (i) of the best performing solar cell.

Table 1) hence, they have more available electrons resulting in increasing the basicity in CS.

Additionally, these synthesized carbon nanomaterials are utilized in unison with TiO$_2$ nanostructures for DSSCs. The synthesis and characterization of these TiO$_2$ nanostructures were reported earlier by our group.[24,25] Kim et al. have reported graphitic films embedded onto TiO$_2$ photoanodes for highly efficient DSSC on the lower, upper, and both sides of the photoanode film with the highest recorded efficiency of 5.21% for the latter.[3] In our study, high performing oval grain morphology anatase TiO$_2$ prepared at subzero degree temperature (−40 °C TiO$_2$) and a ZnO-doped TiO$_2$ (ZnO-TiO$_2$) heterojunction solid sphere were incorporated along with the synthesized CS and CNB in different combinations to optimize maximum performance of the DSSC device. The photoanodes were prepared by mixing in a mortar pestle with ethylene glycol and α terpineol and screen printed on the FTOs (fluorine doped tin oxide glass, 7−12 Ω/sq). The performance of fabricated DSSCs revealed that the overall efficiency of the device showed great improvement in its performance as given in Table 2. A graph showing CS and CNB in varying degree of loading percentages with both ZnO−TiO$_2$ and −40 °C TiO$_2$ is given in Figure 5a,b with their respective photoconversion efficiency calculated from the DSSC device.

To understand better, loading amount was optimized for highest yield, by varying CNB and CS loading 0.5%, 1%, 2% and 5% for both ZnO doped TiO$_2$ and TiO$_2$ synthesized at −40 °C as shown in Figure 5c−f. It can be observed that the

0.5% loading of CNB and CS with both the nanomaterials showed the highest efficiency among all with high current density nearly 20 mA/cm^2. The evident increase in the V_{OC} and J_{SC} strongly suggests the reduced charge recombination and improvement in the charge collection and transport of charge carrier efficiency in the suggested photoanode composition.[5] Additionally, the increased efficiency can be a cumulative factor of the increased surface area leading to better absorption of dye and efficient trapping of photons. This can be attributed to the spherical morphology increasing the pathway and scattering of light. Thus, the measured current density is highly influenced by the amount of dye absorbed over the active area of the fabricated photoanode. A comparative concentration of the amount of dye loaded for the various combinations of photoanode is tabulated in Table S2.

The amount of the dye loaded was calculated by measuring the dye deloaded/desorbed from the photoanode using UV−vis spectra (Figure S3). It was observed that DSSC fabricated using the 0.5% CS_ZnO_TiO$_2$ photoanode showed the highest efficiency of 10.40% among all the other combinations of photoanodes displaying maximum concentration (3.25×10^{-10} M/cm^2) of dye adsorption as can be seen from Table S2. In addition to this, the EIS study was done to investigate the electron transport properties of the system, and its subsequent fitting of the Nyquist plots (Figure 5h) are given in Table 2 and Table S3. Here, R_S is the series resistance, R_1 and R_2 represent the counter electrode and electrolyte charge transfer resistance, respectively, and C_{SC} and C_T represent the chemical
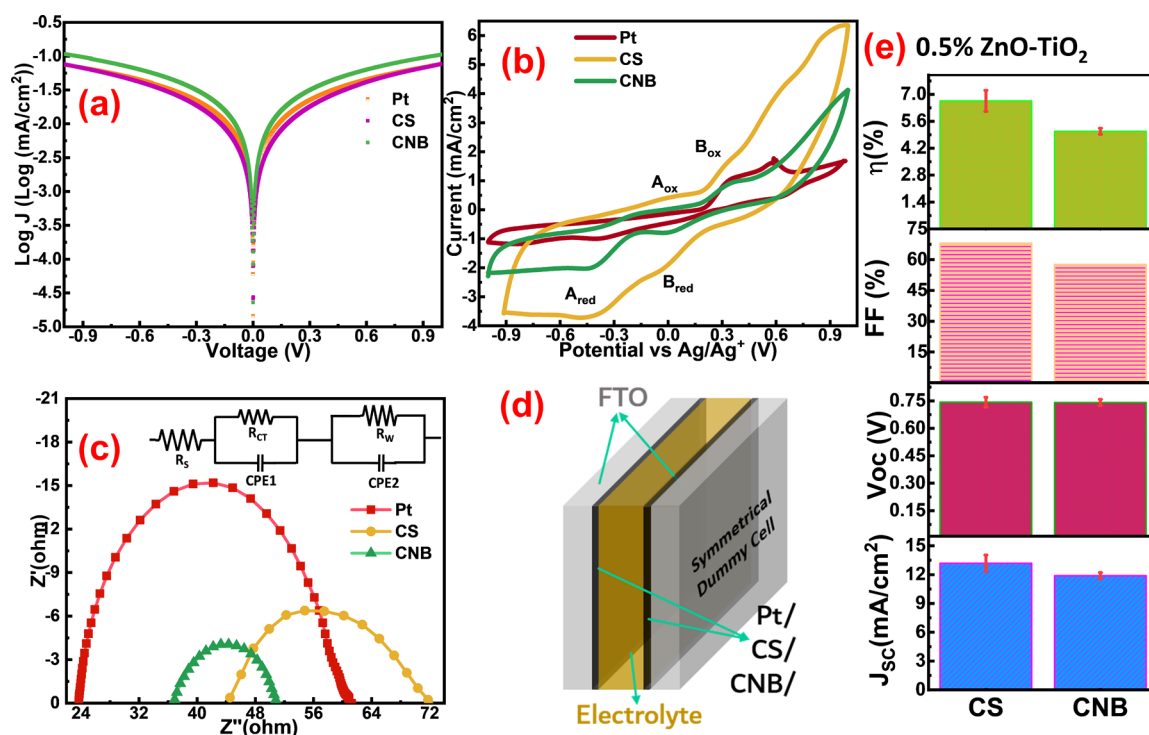
Figure 6. (a) Tafel plot and (b) cyclic voltammetry curves at 20 mV/s scan rate. (c) Nyquist plot with its equivalent circuit diagram (inset) of dummy cells (consists of FTO coated Pt/CS/CNB sandwiched together and filled with 150 mM electrolyte, the active area of which was 0.25 cm^2): R_s, series resistance; R_{ct}, R_w, charge transfer resistance; CPE, constant phase element. (d) Schematic of symmetrical dummy cell constructed using the synthesized carbon nanomaterials and Pt. (e) Illustrative bar graph representation summarizing DSSC performance with CNB and CS as a counter electrode.

capacitance and the Pt- electrolyte capacitance. τ represents the recombination lifetimes of the electrons involved in the process and is calculated from the Bode plot in Figure 5i. The equivalent circuit model best fitted to the Nyquist plot is given in Figure 5g. It is observed that the charge transfer resistance in the TiO$_2$/dye/electrolyte interface is greatly reduced for 0.5% CS and ZnO−TiO$_2$ composite photoanode. It is observed that the charge transfer resistance between the TiO$_2$/dye/electrolyte interface and the charge transport resistance at the Pt counter electrode is decreased for the 0.5% CS + ZnO/TiO$_2$. This along with good conductivity of the carbon increases the electron transport in the fabricated device enhancing the overall photoconversion efficiency (PCE). Moreover, the concoction of high surface area carbon nanomaterials and different forms of TiO$_2$ formulate a good point contact and a uniform homogeneous compact layer between the photoanode and FTO glass substrate, providing an overall increase in PCE.

Furthermore, the prepared CNB and CS were used as a counter electrode in DSSC with the highest performing 0.5% ZnO/TiO$_2$ as the photoanode; the preparation method is given in the experimental section. The exchange and limiting current density, J_o and J_{lim} are defined by the sharp slope and the horizontal trend in the Tafel curve as shown in Figure 6a. It can be observed that the slope is highest for CNB indicating highest J_o in the CNB material and is in accordance with that of the EIS data showing the smallest R_{ct} for CNB. Comparable results were observed for the Pt and CS samples. To further realize the efficiency as catalytic materials for the counter electrode in DSSC, electrochemical properties measurements such as CV and electrochemical impedance measurements were performed (see Figure 6b,c). The prepared carbon samples along with N dopant and good porosity gave a huge

advantage for efficient diffusion of the ions for proper electrocatalytic reaction.[23]

In this study both CNB and CS were subjected to catalytic I$_3^-$ reduction and compared with the Pt counterpart. It can be seen from Figure 6b that the current density is superior for both the carbon nanospheres with CS showing the highest followed by CNB and Pt. However, Pt shows prominent peaks unlike the carbon counter parts which is an indication of the presence of capacitive current. It can also be inferred that there are two prominent oxidation and reduction peaks with the peak to peak ratio, E_{PP} (potential difference between cathodic and anodic peak) calculated in order as CNB < CS < Pt. The oxidation and the reduction peaks correspond to redox activity of the electrolyte as I$_2$ to I$_3^-$ and I$_3^-$ to I$^-$.[44] The reduced E_{PP} and high current density in the carbon nanomaterials suggest the improved activity for catalytically reducing I$_3^-$ to I$^-$ and improved capacitive behavior attributed to high current density. This could be a combined effect of the high specific surface area accompanied by good porosity of the synthesized nanomaterials and also the conceivable improvement in the thickness of the counter electrodes. An illustrative bar graph representation summarizing the observed J_{SC}, V_{OC}, FF, and PCE (η) of the fabricated DSSC devices with CNB and CS as a counter electrode with 0.5% ZnO-TiO$_2$ is shown in Figure 6e. Although, similar V_{OC} values were observed for both nanomaterials, higher FF and J_{SC} were observed which led to the increase in efficiency for CS-based devices.

The electrochemical impedance study was carried out to understand the effect of charge transport. The Nyquist plot in Figure 6c shows the charge transport and transfer activities in the symmetrical dummy cell (schematic in Figure 6d). The Nyquist plot is fitted according to the equivalent circuit
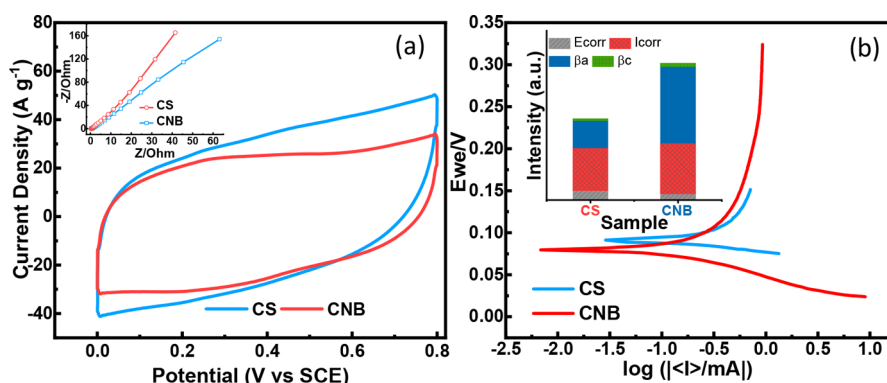
Figure 7. (a) Cyclic voltammetry plots (0.1 mM Na$_2$SO$_4$, applied voltage 0−0.8 V and scan rate 100 mV/s) with the inset plot shows Nyquist plot and (b) Tafel curves with inset bar graph summarizing Tafel parameters and other electrokinetic parameters (Ecorr corrosion potential (mV), Icorr corrosion current (μA), βa anodic and βc cathodic β Tafel constant (mV)) of CS and CNB.

diagram given in the inset of Figure 6c. The calculated charge transfer resistance, R_{ct} was found to be 7 Ω cm^{-2}, 57 Ω cm^{-2}, and 30 Ω cm^{-2}, respectively, for CNB, CS, and Pt. The lower R_{ct} could be attributed to the faster charge transfer process due to the catalytically active large active electrode area.

The synthesized CS and CNB were analyzed as potential materials for its energy storage properties by electrochemical characterizations such as cyclic voltammetry (CV), impedance, and Tafel studies. All the electrochemical studies were performed using three electrode configurations in 0.1 mM Na$_2$SO$_4$ aqueous electrolyte. Figure 7a and Figure S4a,b shows the CV curve obtained from CS and CNB at 100 mV/s and at various scan rates. It was observed that both CS and CNB exhibited near rectangular-shaped curves without any prominent redox potential peaks, indicating a double-layer capacitive behavior, good electrochemical reversibility, and high-power characteristics.

The current density and area under the CV curve for CS are apparently much higher than the CNB at the 100 mV/s scan rate which leads to high specific capacitance (577 F/g) compared to CNB (458 F/g). Inset of Figure 7a is the Nyquist plots of CS and CNB electrodes in the frequency range from 10 Hz to 10 kHz. The impedance spectra show semicircles in the high frequency, an anamorphic semicircle in the medium frequency, and straight lines nearly vertical to the real axis in the low-frequency range. The ideal capacitor always exhibits a vertical line at low frequency.[14,23] The absence of semicircles of supercapacitors is attributed to high charge conductivity that occurs at the electrode surface. At high frequency, the CS electrode has much smaller charge-transfer resistance (almost straight line), suggesting the fast charge transfer and less recombination. However, semicircular-like plots at low frequencies were observed for the electrode with CNB, a result of the slow ion diffusion behavior. Additionally, the improved specific capacitance for CS is attributed to its high specific surface area and e$^-$ transport path, highly conducting C in solid sphere with high effective surface area increases its contact with the electrolyte.

The Tafel plot is used to quantify the polarization results, and it gives the corrosion rate directly. Tafel plots of CS and CNB are shown in Figure 7b, and Tafel parameters and other electrokinetic parameters are summarized in the inset of Figure 7b. The anodic polarization profiles inferred the material dissolution behavior in aggressive media. All the measurements were performed in Na$_2$SO$_4$ solution at the open circuit potential of the respective electrodes. The corrosion potential

value of the electrode was shifted to more positive with a corresponding hollow morphology. Such results suggest that both surfaces, inner and outer, were responsible for these values.

■ CONCLUSION

In summary, highly homogeneous nitrogen-enriched carbon nanospheres as well as carbon nanobubbles were successfully synthesized by a modified Stöber reaction route, and a comparative study on the performance of these nanomaterials as electrode materials for DSSCs, supercapacitors, and CO$_2$ adsorption was performed. Additionally, a systematic study on the integration of highly efficient TiO$_2$ and ZnO as composite photoanode material was performed. When CS and CNB nanomaterials were applied as a DSSC photoanode with TiO$_2$/ZnO heterostructures, the fabricated devices showed improved P−V performance with a remarkable efficiency of 10.40%, excellent point contact, and conductivity. The improved current density, open circuit potential, and the overall efficiency was found to be due to reduced charge recombination, increment in the charge collection, and improvement in the transport of charge carriers through composite photoanode. The structure of the CS nanomaterial offered a much larger surface area for effective capture of CO$_2$ even at low pressure. Electrochemical studies of CNB and CS showed reduced E_{PP} and high current density; suggesting the improved catalytic activity for reducing I$_3^-$ to I$^-$ and good capacitive behavior due to high current density. Both CS and CNB exhibited a near rectangular-shaped CV curve without any prominent redox potential peaks that indicated the double-layer capacitive behavior, good electrochemical reversibility, and high-power characteristics essential for the supercapacitor application. We successfully established our proposition with various characterization techniques and applications that solid CS with larger size and higher surface area yield better output in CO$_2$ capture and photoconversion efficiency, and act as a potential nanomaterial for supercapacitor application. The current investigation is anticipated to open up new possibilities for the design and fabrication of homogeneous multifunctional carbon nanostructures for application in various energy conversion and storage devices.

■ ASSOCIATED CONTENT

Supporting Information

The Supporting Information is available free of charge at https://pubs.acs.org/doi/10.1021/acsanm.0c00402.

TGA curve, UV−vis spectra of the deloaded dyes, CV curves and FTIR of CS and CNB; table detailing the surface porosity details from N_2 BET data and CO_2 adsorption data; tabulation of the dye concentration obtained from the UV−vis of the deloaded dye; table of photovoltaic data of the various photoanode with different compositions with CNB and CS in composition with various ZnO-TiO$_2$ and −40 TiO$_2$ (PDF)

■ AUTHOR INFORMATION

Corresponding Author

Rakesh K. Sharma − *Sustainable Materials and Catalysis Research Laboratory (SMCRL), Department of Chemistry, Indian Institute of Technology Jodhpur, Jodhpur, Rajasthan 342037, India;* ⓘ orcid.org/0000-0002-0984-8281; Email: rks@iitj.ac.in

Authors

Devika Laishram − *Sustainable Materials and Catalysis Research Laboratory (SMCRL), Department of Chemistry, Indian Institute of Technology Jodhpur, Jodhpur, Rajasthan 342037, India;* ⓘ orcid.org/0000-0001-6953-8309

Kiran P. Shejale − *Sustainable Materials and Catalysis Research Laboratory (SMCRL), Department of Chemistry, Indian Institute of Technology Jodhpur, Jodhpur, Rajasthan 342037, India; Department of Metallurgical Engineering and Materials Science, Indian Institute of Technology Bombay, Mumbai, Maharashtra 400076, India;* ⓘ orcid.org/0000-0002-3464-1557

R. Krishnapriya − *Sustainable Materials and Catalysis Research Laboratory (SMCRL), Department of Chemistry, Indian Institute of Technology Jodhpur, Jodhpur, Rajasthan 342037, India;* ⓘ orcid.org/0000-0002-9275-5878

Complete contact information is available at:
https://pubs.acs.org/10.1021/acsanm.0c00402

Author Contributions

‡D.L. and K.P.S. contributed equally.

Notes

The authors declare no competing financial interest.

■ REFERENCES

(1) Dai, L.; Xue, Y.; Qu, L.; Choi, H.-J.; Baek, J.-B. Metal-Free Catalysts for Oxygen Reduction Reaction. *Chem. Rev.* **2015**, *115* (11), 4823−4892.

(2) Mehmood, U.; Malaibari, Z.; Rabani, F. A.; Rehman, A. U.; Ahmad, S. H. A.; Atieh, M. A.; Kamal, M. S. Photovoltaic Improvement and Charge Recombination Reduction by Aluminum Oxide Impregnated MWCNTs/TiO$_2$ Based Photoanode for Dye-sensitized Solar Cells. *Electrochim. Acta* **2016**, *203*, 162−170.

(3) Jang, Y. H.; Xin, X.; Byun, M.; Jang, Y. J.; Lin, Z.; Kim, D. H. An Unconventional Route to High-efficiency Dye-sensitized Solar Cells via Embedding Graphitic Thin Films into TiO$_2$ Nanoparticle Photoanode. *Nano Lett.* **2012**, *12* (1), 479−85.

(4) Yen, M.-Y.; Hsiao, M.-C.; Liao, S.-H.; Liu, P.-I.; Tsai, H.-M.; Ma, C.-C. M.; Pu, N.-W.; Ger, M.-D. Preparation of Graphene/multi-walled Carbon Nanotube Hybrid and its Use as Photoanodes of Dye-sensitized Solar Cells. *Carbon* **2011**, *49* (11), 3597−3606.

(5) Yu, J.; Fan, J.; Cheng, B. Dye-sensitized Solar Cells Based on Anatase TiO$_2$ Hollow Spheres/carbon Nanotube Composite Films. *J. Power Sources* **2011**, *196* (18), 7891−7898.

(6) Liu, X.; Zhang, J.; Guo, S.; Pinna, N. Graphene/N-doped Carbon Sandwiched Nanosheets with Ultrahigh Nitrogen Doping for Boosting Lithium-ion Batteries. *J. Mater. Chem. A* **2016**, *4* (4), 1423−1431.

(7) Brown, P.; Takechi, K.; Kamat, P. V. Single-Walled Carbon Nanotube Scaffolds for Dye-Sensitized Solar Cells. *J. Phys. Chem. C* **2008**, *112*, 4776−4782.

(8) Yen, C.-Y.; Lin, Y.-F.; Hung, C.-H.; Tseng, Y.-H.; Ma, C.-C. M.; Chang, M.-C.; Shao, H. The Effects of Synthesis Procedures on the Morphology and Photocatalytic Activity of Multi-walled Carbon Nanotubes/TiO$_2$ Nanocomposites. *Nanotechnology* **2008**, *19* (4), 045604.

(9) Brennan, L. J.; Byrne, M. T.; Bari, M.; Gun'ko, Y. K. Carbon Nanomaterials for Dye-Sensitized Solar Cell Applications: A Bright Future. *Adv. Energy Mater.* **2011**, *1* (4), 472−485.

(10) Yun, Y. S.; Cho, S. Y.; Kim, H.; Jin, H.-J.; Kang, K. Ultra-Thin Hollow Carbon Nanospheres for Pseudocapacitive Sodium-Ion Storage. *ChemElectroChem* **2015**, *2* (3), 359−365.

(11) Xu, C.; Niu, D.; Zheng, N.; Yu, H.; He, J.; Li, Y. Facile Synthesis of Nitrogen-Doped Double-Shelled Hollow Mesoporous Carbon Nanospheres as High-Performance Anode Materials for Lithium Ion Batteries. *ACS Sustainable Chem. Eng.* **2018**, *6* (5), 5999−6007.

(12) Xu, J.; Ma, C.; Cao, J.; Chen, Z. Facile synthesis of Core-shell Nanostructured Hollow Carbon Nanospheres@nickel Cobalt Double Hydroxides as High-performance Electrode Materials for Supercapacitors. *Dalton Trans* **2017**, *46* (10), 3276−3283.

(13) Li, Q.; Guo, J.; Xu, D.; Guo, J.; Ou, X.; Hu, Y.; Qi, H.; Yan, F. Electrospun N-Doped Porous Carbon Nanofibers Incorporated with NiO Nanoparticles as Free-Standing Film Electrodes for High-Performance Supercapacitors and CO$_2$ Capture. *Small* **2018**, *14* (15), No. e1704203.

(14) Wickramaratne, N. P.; Xu, J.; Wang, M.; Zhu, L.; Dai, L.; Jaroniec, M. Nitrogen Enriched Porous Carbon Spheres: Attractive Materials for Supercapacitor Electrodes and CO$_2$ Adsorption. *Chem. Mater.* **2014**, *26* (9), 2820−2828.

(15) Zhu, G.; Wang, H.; Xu, H.; Zhang, Q.; Sun, H.; Zhang, L. Nitrogen-doped Carbon Microspheres Counter Electrodes for Dye-sensitized Solar Cells by Microwave Assisted Method. *RSC Adv.* **2016**, *6* (63), 58064−58068.

(16) Sun, L.; Ma, T.; Zhang, J.; Guo, X.; Yan, C.; Liu, X. Double-shelled Hollow Carbon Spheres Confining Tin as High-Performance Electrodes for Lithium Ion Batteries. *Electrochim. Acta* **2019**, *321*, 134672.

(17) Yuan, X.; An, N.; Zhu, Z.; Sun, H.; Zheng, J.; Jia, M.; Lu, C.; Zhang, W.; Liu, N. Hierarchically Porous Nitrogen-doped Carbon Materials as Efficient Adsorbents for Removal of Heavy Metal Ions. *Process Saf. Environ. Prot.* **2018**, *119*, 320−329.

(18) Hu, Y.; Gao, X. J.; Zhu, Y.; Muhammad, F.; Tan, S.; Cao, W.; Lin, S.; Jin, Z.; Gao, X.; Wei, H. Nitrogen-Doped Carbon Nanomaterials as Highly Active and Specific Peroxidase Mimics. *Chem. Mater.* **2018**, *30* (18), 6431−6439.

(19) Fellinger, T. P.; Hasche, F.; Strasser, P.; Antonietti, M. Mesoporous Nitrogen-doped Carbon for the Electrocatalytic Synthesis of Hydrogen Peroxide. *J. Am. Chem. Soc.* **2012**, *134* (9), 4072−5.

(20) Fan, M.; Pan, X.; Lin, W.; Zhang, H., Carbon-Covered Hollow Nitrogen-Doped Carbon Nanoparticles and Nitrogen-Doped-Carbon-

Covered Hollow Carbon Nanoparticles for Oxygen Reduction. *ACS Appl. Nano Mater.* **2020.** DOI: 10.1021/acsanm.0c00222

(21) Chen, H.; Sun, F.; Wang, J.; Li, W.; Qiao, W.; Ling, L.; Long, D. Nitrogen Doping Effects on the Physical and Chemical Properties of Mesoporous Carbons. *J. Phys. Chem. C* **2013,** *117* (16), 8318−8328.

(22) Du, J.; Zhang, Y.; Wu, H.; Hou, S.; Chen, A. N-doped Hollow Mesoporous Carbon Spheres by Improved Dissolution-capture for Supercapacitor. *Carbon* **2020,** *156,* 523−528.

(23) Wang, L.; Gao, Z.; Chang, J.; Liu, X.; Wu, D.; Xu, F.; Guo, Y.; Jiang, K. Nitrogen-Doped Porous Carbons As Electrode Materials for High-Performance Supercapacitor and Dye-Sensitized Solar Cell. *ACS Appl. Mater. Interfaces* **2015,** *7* (36), 20234−44.

(24) Shejale, K. P.; Laishram, D.; Sharma, R. K. High-performance Dye-sensitized Solar Cell Using Dimensionally Controlled Titania Synthesized at Sub-zero Temperatures. *RSC Adv.* **2016,** *6* (28), 23459−23466.

(25) Shejale, K. P.; Laishram, D.; Gupta, R.; Sharma, R. K. Zinc Oxide-Titania Heterojunction-based Solid Nanospheres as Photoanodes for Electron-Trapping in Dye-Sensitized Solar Cells. *Energy Technology* **2017,** *5* (3), 489−494.

(26) Mehmood, U.; Ul Haq Khan, A.; Ali Qaiser, A.; Bashir, S.; Younas, M. Nanocomposites of carbon allotropes with TiO_2 as effective photoanodes for efficient dye-sensitized solar cells. *Mater. Lett.* **2018,** *228,* 125−128.

(27) Shaikh, J. S.; Shaikh, N. S.; Mali, S. S.; Patil, J. V.; Pawar, K. K.; Kanjanaboos, P.; Hong, C. K.; Kimd, J. H.; Patil, J. V. Nano-architectures in dye-sensitized solar cells: metal oxides, oxide perovskites and carbon-based materials. *Nanoscale* **2018,** *10,* 4987−5034.

(28) Fuertes, A. B.; Valle-Vigon, P.; Sevilla, M. One-step synthesis of silica@resorcinol-formaldehyde spheres and their application for the fabrication of polymer and carbon capsules. *Chem. Commun. (Cambridge, U. K.)* **2012,** *48* (49), 6124−6.

(29) Stöber, W.; Fink, A.; Bohn, E. Controlled growth of monodisperse silica spheres in the micron size range. *J. Colloid Interface Sci.* **1968,** *26* (1), 62−69.

(30) ElKhatat, A. M.; Al-Muhtaseb, S. A. Advances in Tailoring Resorcinol-Formaldehyde Organic and Carbon Gels. *Adv. Mater.* **2011,** *23* (26), 2887−2903.

(31) Anh Cao, K. L.; Arif, A. F.; Kamikubo, K.; Izawa, T.; Iwasaki, H.; Ogi, T. Controllable Synthesis of Carbon-Coated SiOx Particles through a Simultaneous Reaction between the Hydrolysis-Condensation of Tetramethyl Orthosilicate and the Polymerization of 3-Aminophenol. *Langmuir* **2019,** *35* (42), 13681−13692.

(32) Wang, X.-D.; Shen, Z.-X.; Sang, T.; Cheng, X.-B.; Li, M.-F.; Chen, L.-Y.; Wang, Z.-S. Preparation of spherical silica particles by Stöber process with high concentration of tetra-ethyl-orthosilicate. *J. Colloid Interface Sci.* **2010,** *341* (1), 23−29.

(33) Liu, J.; Qiao, S. Z.; Liu, H.; Chen, J.; Orpe, A.; Zhao, D.; Lu, G. Q. Extension of The Stöber Method to the Preparation of Monodisperse Resorcinol-Formaldehyde Resin Polymer and Carbon Spheres. *Angew. Chem., Int. Ed.* **2011,** *50* (26), 5947−5951.

(34) Bogush, G. H.; Tracy, M. A.; Zukoski, C. F. Preparation of monodisperse silica particles: Control of size and mass fraction. *J. Non-Cryst. Solids* **1988,** *104* (1), 95−106.

(35) Lowell, S.; Shields, J. E.; Thomas, M. A.; Thommes, M. *Characterization of Porous Solids and Powders_ Surface Area, Pore Size and Density*; Kluwer Academic Publishers: Netherlands, 2004.

(36) Xu, F.; Tang, Z.; Huang, S.; Chen, L.; Liang, Y.; Mai, W.; Zhong, H.; Fu, R.; Wu, D. Facile Synthesis of Ultrahigh-surface-area Hollow Carbon Nanospheres for Enhanced Adsorption and Energy Storage. *Nat. Commun.* **2015,** *6* (1), 7221.

(37) Liu, W.; Mei, J.; Liu, G.; Kou, Q.; Yi, T.; Xiao, S. Nitrogen-Doped Hierarchical Porous Carbon from Wheat Straw for Supercapacitors. *ACS Sustainable Chem. Eng.* **2018,** *6* (9), 11595−11605.

(38) Liu, X.; Song, P.; Hou, J.; Wang, B.; Xu, F.; Zhang, X. Revealing the Dynamic Formation Process and Mechanism of Hollow Carbon

Spheres: From Bowl to Sphere. *ACS Sustainable Chem. Eng.* **2018,** *6* (2), 2797−2805.

(39) Ding, S.; Liu, B.; Zhang, C.; Wu, Y.; Xu, H.; Qu, X.; Liu, J.; Yang, Z. Amphiphilic Mesoporous Silica Composite Nanosheets. *J. Mater. Chem.* **2009,** *19* (21), 3443−3448.

(40) Liu, L.; Xie, Z.-H.; Deng, Q.-F.; Hou, X.-X.; Yuan, Z.-Y. One-pot Carbonization Enrichment of Nitrogen in Microporous Carbon Spheres for Efficient CO_2 Capture. *J. Mater. Chem. A* **2017,** *5* (1), 418−425.

(41) Li, M.; Cheng, J. P.; Wang, J.; Liu, F.; Zhang, X. B. The Growth of Nickel-manganese and Cobalt-manganese Layered Double Hydroxides on Reduced Graphene Oxide for Supercapacitor. *Electrochim. Acta* **2016,** *206,* 108−115.

(42) Xia, K.; Yu, Y.; Li, Y.; Li, S.; Wang, Y.; Wang, G.; Zhang, H.; Chen, A. Controllable Synthesis of Nitrogen-doped Hollow Carbon Nanospheres with Dopamine as Precursor for CO_2 Capture. *RSC Adv.* **2016,** *6* (94), 91557−91561.

(43) Xing, W.; Liu, C.; Zhou, Z.; Zhang, L.; Zhou, J.; Zhuo, S.; Yan, Z.; Gao, H.; Wang, G.; Qiao, S. Z. Superior CO_2 Uptake of N-doped Activated Carbon through Hydrogen-bonding Interaction. *Energy Environ. Sci.* **2012,** *5* (6), 7323−7327.

(44) Krishnapriya, R.; Praneetha, S.; Rabel, A. M.; Vadivel Murugan, A. Energy Efficient, One-step Microwave-solvothermal Synthesis of a Highly Electro-catalytic Thiospinel $NiCo_2S_4$/graphene Nanohybrid as a Novel Sustainable Counter Electrode Material for Pt-free Dye-sensitized Solar Cells. *J. Mater. Chem. C* **2017,** *5* (12), 3146−3155.